Published in final edited form as:
Appl Opt. 2009 March 1; 48(7): 1328–1336.

Quantitative fluorescence tomography with functional and structural *a priori* information

Yuting Lin, **Han Yan**, **Orhan Nalcioglu**, and **Gultekin Gulsen**[*]
Center for Functional Onco-Imaging, University of California, Irvine, Irvine, California 92697, USA

Abstract

We demonstrate the necessity of functional and structural *a priori* information for quantitative fluorescence tomography (FT) with phantom studies. Here the functional *a priori* information is defined as the optical properties of the heterogeneous background that can be measured by a diffuse optical tomography (DOT) system. A CCD-based noncontact hybrid FT/DOT system that could take measurements at multiple views was built. Multimodality phantoms with multiple compartments were constructed and used in the experiments to mimic a heterogeneous optical background. A 3:6 mm diameter object deeply embedded in a heterogeneous optical background could be localized without any *a priori* information, but the recovered fluorophore concentration only reached one tenth of the true concentration. On the other hand, the true fluorophore concentration could be recovered when both functional and structural *a priori* information is utilized to guide and constrain the FT reconstruction algorithm.

1. Introduction

Fluorescence imaging is one of the molecular imaging modalities that have many applications ranging from basic science to clinical research. In this technique, contrast is provided by exogenous fluorescence agents that are used to label cells or proteins. There are two main ways of labeling cells, namely, direct and indirect labeling. Cells or proteins under investigation can be directly labeled by conjugating fluorophores to a primary antibody, antibody fragment, peptide, or ligand. Alternatively, a fluorescent protein can be used as a reporter to study gene expression and regulation. *In vitro* imaging techniques such as fluorescence microscopy have been used extensively to look at the immunofluorescence staining or green fluorescence protein expression in molecular cell biology. Recently, *in vivo* fluorescence imaging techniques have been developed using the same cell-labeling concept [1,2]. After all, visualization of biological processes at amolecular level in living subjects holds promises in many clinical applications such as early cancer detection, monitoring cell-based therapy by following the cell migration, and validating drug delivery [2–6]. As a commonly used tool for *in vivo* imaging of small animals, conventional planar fluorescence imaging systems create a projectional two-dimensional fluorescence distribution map using relatively simple and fast instrumentation [7,8]. However, due to the highly diffusive nature of the photon propagation in tissue, it is difficult to recover the depth, size, and fluorophore concentration information accurately from a projection image. On the other hand, fluorescence tomography (FT) can provide cross-sectional or full three-dimensional (3D) images, although the quantitative accuracy in the recovered fluorophore concentration is still low [9–11]. In FT, first the propagation of the excitation light should be modeled from the boundary to the fluorophore embedded inside the

---

[*]Corresponding author: ggulsen@uci.edu.

OCIS codes: 170.3010, 170.6960.

medium. Then propagation of the emitted light should be modeled from the fluorophore to the detectors located at the boundary of the medium. Consequently, the spatial distribution and the concentration of the fluorophore can be reconstructed computationally by matching the photon distribution predicted by the model and the experimental photon measurements.

FT is an extension of another widely studied optical imaging modality, diffuse optical tomography (DOT), which uses near-infrared light to recover the optical absorption and scattering maps of the medium under investigation. DOT has been applied for animal as well as clinical breast and brain imaging [12–15]. The inverse problem is ill posed and underdetermined for both DOT and FT due to the high scattering nature of the tissue and limited number of measurements acquired from the boundary of the medium [16]. As a result, both modalities suffer from the low spatial resolution and cannot recover the optical parameters accurately. Structural *a priori* information has been found to be particularly effective in improving the quantitative accuracy by guiding and constraining the reconstruction algorithm. Meanwhile, simulation and experimental studies validated that the structural *a priori* information improves the DOT reconstruction significantly [14,17–20].

Although this approach has been found effective for DOT, it alone would not be enough to recover the true fluorophore concentration using the FT technique. The main reason for this is the necessity of the knowledge of the background optical property map for proper modeling of the light propagation at the excitation and the emission wavelengths. Hence here we categorize *a priori* information into two types, namely, functional and structural *a priori* information. The functional *a priori* information is defined as the background optical properties of the heterogeneous medium, and structural *a priori* is defined as the anatomical information of the object. In essence, the background optical absorption map obtained using DOT can be utilized as the functional *a priori* information during FT reconstruction. As a result, light propagation at both excitation and emission wavelengths can be predicted more accurately when the background optical property map is available.

Published studies have not systematically investigated the quantitative improvement in the FT reconstruction in a heterogeneous background with both structural and functional *a priori* information. Some of those studies emphasize the importance of the structural *a priori* information [21–24], while others emphasize the significance of the functional *a priori* information [25–27]. We recently conducted simulation studies to show that both functional and structural *a priori* information is essential for the accurate recovery of fluorophore concentration of small inclusions deeply embedded in a heterogeneous medium.

Following the simulation studies, we carried out phantom studies to demonstrate the necessity of both types of *a priori* information for quantitative FT. For this purpose, we constructed multimodality phantoms with multiple compartments to mimic background optical heterogeneity. Indocyanine Green (ICG), which is the only FDA-approved fluorescence contrast agent, was used as the fluorophore. The background optical heterogeneity information was obtained with DOT measurements at both excitation and emission wavelengths and used as the functional *a priori* information. Magnetic resonance imaging (MRI) contrast agent Gd-DTPA, a widely used agent in the dynamic contrast-enhanced (DCE) MRI, was also added to different compartments at different amounts. The phantom composition was determined from the T1-weighted anatomical magnetic resonance (MR) images and used as the structural *a priori* information for the FT reconstruction. Here we report the results of these phantom studies. These experimental studies confirmed that the fluorophore concentration of an inclusion deeply embedded inside a heterogeneous background could only be recovered accurately when both functional and structural *a priori* information was available.

2. Method

A. Image Reconstruction

The light propagation in tissue is described by a coupled diffusion equation in the continuous wave domain:

$$\nabla\cdot[D_x(r)\nabla\Phi_x(r)]-[\mu_{ax}(r)+\mu_{af}(r)]\Phi_x(r)=-q0(r), \tag{1}$$

$$\nabla\cdot[D_m(r)\nabla\Phi_m(r)]-[\mu_{\mathrm{am}}(r)]\Phi_m(r)=-\Phi_x(r)\eta\mu_{\mathrm{af}}(r), \tag{2}$$

where $\Phi_x(r)$ and $\Phi_m(r)$ (Wmm^{-2}) are the photon density for the excitation and emission light, respectively, and $D_{x,m}(r)(\mathrm{mm}^{-1})$ denotes the diffusion coefficient, which is defined by $D_{x,m} = 1/3(\mu_{ax,m} + \mu_{s}'{}_{x,m})$. The reduced scattering and the absorption coefficients of the medium are represented as $\mu_{s}'{}_{x,m}(\mathrm{mm}^{-1})$ and $\mu_{ax,m}(\mathrm{mm}^{-1})$, respectively. The absorption coefficients are expected to differ at excitation and emission wavelengths due to the diverse spectral dependence of the absorption of each individual tissue chromophore. Absorption coefficient due to fluorophore $\mu_{af}(r)$ is directly related to the ICG concentration by the formula $\mu_{af} = 2{:}3\varepsilon C$, where ε is the extinction coefficient of the fluorophore with the unit of $\mathrm{molar}^{-1}\mathrm{mm}^{-1}$, and C is the concentration of the fluorophore. Quantum yield η is the intrinsic property of the fluorophore and defined as the ratio of the number of photons emitted to the number of photons absorbed. According to the literature, ICG has excitation and emission maxima at 785 and 830 nm, and the ICG extinction coefficient at these wavelengths is 130,000 and 22; 000 molar^{-1} mm^{-1}, respectively [28]. Mean-while, the quantum efficiency of ICG is 0.016.

The Robin boundary condition relates the optical fluence rate to optical flux at the boundary and can be written as

$$\Phi_{x,m}(r)+2AD_{x,m}(r)\frac{\partial\Phi_{x,m}(r)}{\partial n}=0, \tag{3}$$

where n is the direction perpendicular to the boundary, and A is the boundary mismatch parameter and accounts for the light reflection on the boundary surface, which is determined by Fresnel equations. The extrapolated-boundary condition is applied to model the position of the source [29].

The coupled diffusion equation is an elliptical-type partial differential equation (PDE). A numerical solution of this PDE is applied in a finite element method (FEM) framework. The weak form of coupled diffusion Eqs. (1) and (2) can be expressed as

$$\int_\Omega \mathrm{d}\overrightarrow{x}\nabla\varphi\cdot(\mathrm{d}_x\nabla\Phi_x)+\int_\Omega \mathrm{d}\overrightarrow{x}(\mu_{ax}+\mu_{af})\varphi\Phi_x +\frac{1}{2A}\int_{\partial\Omega}\mathrm{d}\overrightarrow{s}\varphi\Phi_x=\int_\Omega \mathrm{d}\overrightarrow{x}\varphi q_0, \tag{4}$$

$$\int_\Omega \mathrm{d}\overrightarrow{x}\nabla\varphi\cdot(D_m\nabla\Phi_m)+\int_\Omega \mathrm{d}\overrightarrow{x}(\mu_{am})\varphi\Phi_m +\frac{1}{2A}\int_{\partial\Omega}\mathrm{d}\overrightarrow{s}\varphi\Phi_m=\int_\Omega \mathrm{d}\overrightarrow{x}\varphi\eta\mu_{af}\Phi_x, \tag{5}$$

where φ is a arbitrary test function. Function $\Phi_{x,m}$ can be expressed as $\Phi_{x,m}=\sum_{j=1}^{N}\xi_{x,mj}\varphi_{j}$, where φ is a basis function for the *j*th node. We choose the piecewise linear function as the basis function. The distribution $D_{x,m}$, $\mu_{x,m}$, and μ_{af} can also be represented as $D_{x,m}=\sum_{k=1}^{N}D_{x,mk}\varphi_{k}$ and $\mu_{\mathrm{ax},m,f}=\sum_{k=1}^{N}\mu_{\mathrm{ax},m,fk}\varphi_{k}$. When the test function is also written as $\varphi=\sum_{x=1}^{N}\varphi_{x}$, the coupled diffusion Eqs. (1) and (2) in the FEM framework is

$$(A_x+B_x+C)\xi_x=Q_x, \quad (A_m+C)\xi_m=Q_m\xi_x, \tag{6}$$

where

$$\begin{aligned}
(A_x)_{\mathrm{ij}} &= \sum_{k=1}^{N} D_{x,k}\int_{\Omega}\mathrm{d} \rightarrow x\varphi_k(\nabla\varphi_i \bullet \nabla_{\varphi_j}) \\
&\quad + \sum_{k=1}^{N}\mu_{x,k}\int_{\Omega}\mathrm{d}x\varphi_k(\varphi_i\varphi_j) \\
(B_x)_{\mathrm{ij}} &= \sum_{k=1}^{N}\mu_{\mathrm{af},k}\int_{\Omega}\mathrm{d} \rightarrow x\varphi_k(\varphi_i\varphi_j) \\
(C)_{\mathrm{ij}} &= \int_{\partial\Omega}\mathrm{d} \rightarrow s(\varphi_i\varphi_j) \\
(A_m)_{\mathrm{ij}} &= \sum_{k=1}^{N} D_{m,k}\int_{\Omega}\mathrm{d} \rightarrow x\varphi_k(\nabla\varphi_i \bullet \nabla\varphi_j) \\
&\quad + \sum_{k=1}^{N}\mu_{m,k}\int_{\Omega}\mathrm{d} \rightarrow x\varphi_k(\varphi_i\varphi_j) \\
(Q_x)_i &= \int_{\Omega}\mathrm{d} \rightarrow x(\varphi_i q_0) \\
(Q_m)_{\mathrm{ij}} &= \sum_{k=1}^{N}\mu_{\mathrm{af},k}\int_{\Omega}\mathrm{d} \rightarrow x\eta\varphi_k(\varphi_i\varphi_j),
\end{aligned}$$

The inverse problem is solved by minimizing the difference between the measured and the calculated data according to the error functions

$$\varepsilon^2(\mu_a)=\sum_{i=1}^{N_s}\sum_{j=1}^{N_d}(\phi_{ij}^{m}-P_{ij}(\mu_a))^2, \tag{7}$$

$$\varepsilon^2(\mu_{af})=\sum_{i=1}^{N_s}\sum_{j=1}^{N_d}(\phi_{ij}^{m}-P_{ij}(\mu_{af}))^2, \tag{8}$$

for the DOT and FT measurements, respectively. Here *i* represents the number of sources, *j* represents the number of detectors, ϕ_{ij}^{m} the measurement, and $P_{ij}(\mu_a)$ and $P_{ij}(\mu_{af})$ represent the flux on the measured point calculated by the forward solver from the spatial distribution of $\mu_{ax,m}$ and μ_{af} . We iteratively update the unknown μ_a and μ_{af} with the Levenberg–Marquardt method by

$$X_{m+1}=X_m+(J^T J+\lambda I)^{-1}(J^T \varepsilon), \tag{9}$$

where $\varepsilon_{\mathrm{ij}}=(\phi_{\mathrm{ij}}^m - P_{\mathrm{ij}})$ and X represents the unknown matrix of $\mu_{ax,m}$ and μ_{af}. The dimension of X is N, and N represents the number of nodes in the FEM mesh. The Jacobian matrix J is calculated with the adjoint method [12]. When the functional *a priori* information is available, we first reconstruct $\mu_{x,m}$ from the DOT data. Then Φ_x is calculated using μ_{x} and is used in the second equation. Following that, μ_{af} is reconstructed using Φ_x and μ_m, which are obtained from the DOT. A homogeneous $\mu_{ax,m}$ or μ_{af} distribution is assumed as the initial guess in the reconstruction process. These values are found by minimizing the difference between the forward solver solution and the measurements. When the structural *a priori* information is available, Laplacian-type *a priori* developed by Yalavarthy *et al.* is used to find the fluorophore concentration for the inclusion and the background [30]. The L matrix can be written as

$$L_{\mathrm{ij}}=\begin{cases} 0 & \text{if } i \text{ and } j \text{ are not in the same region} \\ 1/N_r & i \text{ and } j \text{ are in the same region} \\ 1 & \text{if } i=j \end{cases}, \tag{10}$$

where N_r represents the number of nodes included in one region. Then the updated equation can be expressed as

$$X_{m+1}=X_m+(J^T J+\lambda L^T L)^{-1}(J^T \varepsilon). \tag{11}$$

A fine mesh (4225 nodes and 8192 elements) was used for the forward solver, while a coarse mesh (1089 nodes and 2048 elements) was used for the inverse problem. When the structural *a priori* information is available, 32 nodes were selected to represent the 3:6 mm fluorescence object.

B. Instrumentation

A photograph of the system is shown in Fig. 1(a). A cooled CCD camera (Perkin Elmer, Cold Blue) coupled with a lens focused at the object was used for photon detection. It was fixed on a table 30 cm away from the rotation stage that held the object to be imaged. For the FT measurement, two 830nm bandpass filters (MK Photonics, Albuquerque, New Mexico) were used to eliminate excitation light at 785 nm. A stepper motor controller (National Instruments, NI-7400) and a power driver (National Instruments, NI-7600) were used to control the rotation stage with a computer. The rotation stage allowed measurements to be taken at multiple views. The laser light was sent to the object sequentially from three different directions that were 45° apart from each other; see Fig. 1(b). A computer-controlled fiber-optic switch (DiCon Fiberoptics, Richmond, California) was used to activate any one of the three source locations. It also allowed the selection of the source wavelength. Two different lasers were used in the system, 785nm (75mW, Thorlabs, Newton, New Jersey) and 830nm (150mW, Intelite, Genoa, Nevada). DOT measurements were acquired at both wavelengths. Following that, the first laser was used for the FT measurements to excite the fluorophore ICG (IC-Green, Akorn, Buffalo Grove, Illinois).

C. Phantom Studies

We constructed phantoms with multiple compartments to simulate heterogeneous tissue optical properties. The phantoms were prepared using agarose powder (OmniPur Agarose, Lawrence, Kansas). The Intralipid and India ink were added as optical scatterer and absorber, respectively.

A homogeneous DOT calibration phantom was made with absorption coefficient μ_a = 0:013 mm^{-1} and reduced scattering coefficient μ_s = 1:0 mm^{-1},measured with a frequency-domain DOT system [14]. Another homogeneous FT calibration phantom was also prepared using the ICG as the fluorophore and the absorber. The ICG is difficult to characterize due to its varying absorption spectrum over time. In order to quantify the amount of the ICG in the inclusion, we preserved some sample during the phantom construction and measured the absorption spectrum with a spectrometer (Ocean Optics, USB2000) at the time of the phantom measurements.

For both DOT and FT, images were acquired from eight views (45° apart) for each source position. For each view, a set of 21 virtual detectors was placed uniformly on the corresponding boundary segment and mapped to the CCD [Fig. 2(b)]. For DOT measurements, the CCD integration time for the source positions L1 and L3 and the source position L2 was 50 and 500 ms, respectively [source positions are represented in Fig. 1(b)], while FT measurements were obtained with 1 min integration time for all three source positions.

The calibration procedure was performed for the DOT and the FT separately. For the DOT calibration, a complete set of data was taken and averaged using the homogeneous DOT calibration phantom. This step took data/model mismatch into account. Similarly, the FT calibration was also carried out by taking a complete set of FT measurements using the homogeneous FT calibration phantom.

Three phantoms with increased complexity are investigated in this paper. The first case was designed to validate the performance of the system. The second and third cases were designed to evaluate the effect of the functional and structural *a priori* information on the FT reconstruction. The fluorophore inclusion was embedded in a homogeneous background in the first case, while the inclusions were positioned in a heterogeneous optical background in the second and third cases. The ICG inclusion was placed in a transparent tube.

Case 1—The phantom had a 3:6 mm diameter hole filled with ICG and Intralipid inclusion located 10 mm away from the center of the phantom. The background optical properties were μ_{ax} = 0:013 mm^{-1}, μ_{am} = 0:011 mm^{-1}, and $\mu_{s'x,m}$ = 1:0 mm^{-1}. The ICG concentration in the inclusion was 0:67 μM, which set the absorption coefficient due to the fluorophore in the inclusion to 0:02 mm^{-1}. The diagram of the phantom is shown in Fig. 2(a). The fluorophore concentration map was reconstructed with and without the structural *a priori* information. In addition, we evaluated the effect of the imperfect structural*a priori* information. Therefore the fluorophore concentration map was also reconstructed when the object size was underestimated 10% and when the object location was estimated 3 mm off from the structural images.

Cases 2 and 3—We investigated two more cases where the ICG inclusion was embedded in a heterogeneous medium. The commonly used MR contrast agent, Gd-DTPA, was added to the different compartments of the phantom at different amounts. Consequently, the boundaries of the compartments were obtained from the T1-weighted MR images and used as the structural *a priori* information (see Fig. 3, first row). Both DOT and FT measurements were acquired sequentially. The absorption map of the phantom for both emission and excitation wavelengths were reconstructed using DOT measurements and utilized as the functional *a priori* information. Later, the ICG concentration was reconstructed using four different combinations of the functional and structural *a priori* information as follows:

A. using erroneous absorption coefficient and disregarding the background heterogeneity

B. using reconstructed absorption maps from the DOT measurements as the functional *a priori* information during the FT reconstruction,

C. using erroneous absorption coefficient while disregarding the background heterogeneity and using only the structural *a priori* information for the FT reconstruction, and

D. using reconstructed absorption map as the functional *a priori* information and applying the structural *a priori* information in the FT reconstruction.

In Case 2, the background optical property was kept the same as Case 1. However, heterogeneous optical background was obtained by adding an absorptive inclusion with optical properties of $\mu_{ax} = 0{:}035\ \mathrm{mm}^{-1}$, $\mu_{am} = 0{:}03\ \mathrm{mm}^{-1}$, and $\mu_{s'x,m} = 1{:}0\ \mathrm{mm}^{-1}$. This absorptive inclusion was 14 mm in diameter and located 5 mm offset from the center of the phantom. Meanwhile, the ICG inclusion was 3:6 mm in diameter and 10 mm away from the center of the phantom. It was located outside the absorptive inclusion and had a concentration of 0:67 μM. As a result, the absorption coefficient in the inclusion due to the fluorophore was 0:02 mm^{-1}.

The background optical property for Case 3 was similar to the previous cases. Moreover, an absorptive inclusion was also added with the same optical property as in Case 2. This time the absorber was 25 mm in diameter and 5 mm offset from the center of the phantom. Case 3 was particularly more complex than the other two cases since not only the background was more heterogeneous but also the fluorophore was embedded inside the absorption inclusion. Again, the ICG inclusion had a concentration of 0:67 μM, which set the absorption coefficient due to the fluorophore in the inclusion to 0:02 mm^{-1}. Like-wise, it was 3:6 mm in diameter and 10 mm away from the center of the phantom. Furthermore, the ICG inclusion was located off center inside the absorber.

3. Results

Once calibrated using calibration phantom measurements, both DOT and FT data were used to reconstruct the absorption maps at excitation and emission wavelengths as well as the ICG concentration map. The results for Case 1 are shown in Fig. 2. The diagram of the phantom is illustrated in Fig. 2(a), and the source and detector positions for one view are presented in Fig. 2(b). For Case 1, the optical absorption coefficient of the homogeneous background is estimated from the DOT measurements and used as functional *a priori* information. The reconstructed fluorophore concentration maps with and without the structural *a priori* information are shown in Figs. 2(c) and 2(d), respectively. Meanwhile, the results for Cases 2 and 3 are shown in Fig. 4 and Fig. 5. The T1-weighted MR images of the phantoms are presented in the first column of Fig. 3. The intensity profiles are drawn across the fluorescence inclusion as indicated with the dashed line in the MR images (see Fig. 3, column 2). The recovered absorption maps from the DOT measurements are shown in the third column of Fig. 3. The reconstructed fluorophore concentration maps for four different combinations of the functional and structural *a priori* information are presented in Fig. 4(a)–4(d) and Fig. 5(a)–5(d).

Case 1

In this case, the ICG inclusion is located in a homogeneous background. As shown in Fig. 2 (c), the ICG inclusion can be localized, but the mean reconstructed ICG concentration is only 0:15 μM. The full-width at half-maximum (FWHM) of the reconstructed object is 5 mm. On the other hand, when the structural *a priori* information is utilized, the recovered ICG concentration is 0:66 μM [Fig. 2(d)]. In this case, we demonstrate that hybrid FT/DOT system alone is able to localize the position of the fluorophore, but the concentration is recovered with 77% error. However, when the structural *a priori* information is also used to guide the reconstruction, the true fluorophore concentration can be recovered successfully. Furthermore, when the object size is underestimated by 10%, the recovered fluorophore concentration is overestimated by 13%. In the meantime, when the object location is estimated 3 mm off of the true location, the fluorophore concentration is recovered with a 3% error.

Case 2

The results for Case 2 are shown in Fig. 4. The left column is the recovered fluorophore concentration map for Figs. 4(a)–4(d), while the right column shows the corresponding profiles for the recovered fluorescence object. The structure of the phantom can be seen from the T1-weighted MR anatomical image (first column of Fig. 3). When erroneous absorption coefficient $\mu_{ax} = \mu_{am} = 0{:}01\ \mathrm{mm}^{-1}$ is assumed for the background, and its heterogeneity is disregarded, the fluorophore can be localized, but FWHM of the recovered object in the horizontal direction is 13:4 mm. Besides, the recovered concentration reaches only less than one tenth of the true concentration [Fig. 4(a)]. Meanwhile, the reconstructed absorption map for the employed excitation wavelength is shown in the third column of Fig. 3. Figure 4(b) represents the reconstructed ICG concentration map when the reconstructed absorption maps from the DOT measurements are used as the functional *a priori* information during the FT reconstruction. Although the object can be localized accurately, and the FWHM of the recovered object is reduced to 6:9 mm, the recovered ICG concentration still is not accurate, as shown in Table 1. This result is consistent with our earlier simulation results in the case of small fluorophore size [31]. On the other hand, when the structural *a priori* information alone is applied to the FT inverse solver, and the erroneous absorption coefficient $\mu_{ax} = \mu_{am} = 0{:}01\ \mathrm{mm}^{-1}$ is assigned to the background while disregarding its heterogeneity again, the ICG concentration is recovered with 37% error [Fig. 4(c) and Table 1]. Above all, when both functional and structural *a priori* information are used during the FT reconstruction, the fluorophore concentration is recovered with less than 1% error.

Case 3

This case is more complex than the second case due to the more complicated background optical heterogeneity as well as the positioning of the inclusion in the highly absorptive region, as shown in the MR image for Case 3 (Fig. 3 second row). The results for Case 3 are shown in Fig. 5. Again, the recovered fluorophore concentration map and the profile for the recovered fluorescence object are shown in the left and right columns in Fig. 5, respectively. Similar to the previous cases, when the background is assumed to be homogeneous, and erroneous absorption coefficient $\mu_{ax} = \mu_{am} = 0{:}01\ \mathrm{mm}^{-1}$ is assigned, the fluorophore can be localized, but the FWHM of the recovered object is 10:9 mm. Furthermore, the recovered concentration is much lower than in Case 2, almost 100 times lower than the true concentration [Fig. 5(a) and Table 1]. On the other hand, Fig. 5(b) presents the reconstructed ICG concentration map when the reconstructed absorption maps from the DOT measurement are used as the functional *a priori* information in the FT reconstruction. Similar to Case 2, the fluorophore can be localized, and the FWHM of the recovered object is 8:4 mm, but the ICG concentration is recovered with 80% error. When the structural *a priori* information is applied alone in the FT inverse solver, and the erroneous absorption coefficient $\mu_{ax} = \mu_{am} = 0{:}01\ \mathrm{mm}^{-1}$ is assigned to the background while disregarding its heterogeneity, the ICG concentration is recovered with 87% error [Fig. 4(c) and Table 1]. However, when both functional and structural *a priori* information are used during the FT reconstruction, the fluorophore concentration is again recovered with less than 3% error, as given in Table 1.

4. Discussion and Conclusion

Recently, planar fluorescence imaging has been extensively applied for *in vivo* small animal imaging. At the same time, molecular imaging with fluorescence techniques has emerged in personalized medicine applications [32]. Nevertheless, imaging the distribution of the fluorophores located deep in a highly scattering medium with high quantitative accuracy still requires tomographic imaging techniques rather than projection imaging. Indeed, even though a lesion may be detected in the reconstructed image, the true location, size, and most importantly, the true concentration of the fluorophore cannot be recovered unless proper *a priori* information is available [31,33,34]. A system that can reveal quantitatively accurate fluorophore concentration as an image will have a great potential in a number of applications covering a broad range from stem cell to cancer research.

Until now, a number of groups have explored the improvement in the FT reconstruction when the background optical property is obtained from the DOT measurement. Hervé *et al.* have shown that the fluorophore concentration and location can be recovered more accurately by correcting the attenuation heterogeneity *a priori* to the fluorescence reconstruction [26]. Furthermore, Tan and Jiang also demonstrated that DOT-guided FT can recover the fluorophore concentration more accurately [25]. However, as presented in Cases 2 and 3, even though the background heterogeneity is corrected, a small inclusion deeply embedded inside the medium cannot be recovered accurately. On the other hand, a few previous studies have also used the structural *a priori* information to improve FT reconstruction using phantoms with homogeneous background [24,35]. However, as we presented in Cases 2 and 3, the structural *a priori* information alone is not enough to recover quantitatively accurate fluorophore concentration images if the background is heterogeneous. In this study, we confirm that both functional and structural *a priori* information are crucial to recover the fluorophore concentration accurately especially for a small inclusion embedded in a heterogeneous background. For example, when the functional *a priori* information is applied alone, the reconstructed ICG concentration map is substantially improved particularly for Cases 2 and 3. As illustrated in the Table 1, the recovered ICG concentration in the inclusion improved approximately four and ten times for Cases 2 and 3, respectively. Nevertheless, the error in the recovered ICG concentration in the inclusion is still very high, around 80% for both cases. On the other hand, applying the structural *a priori* alone makes a substantial impact only for Case 2, in which the error in the recovered ICG concentration is reduced to 28%. Please note that the background for the third case is more complex than the other two cases. Accordingly, these results reiterate that the structural *a priori* information alone would not be enough for small inclusions located in a highly heterogeneous background. In any case, only when both functional and structural *a priori* information are applied during FT reconstruction can the fluorophore concentration be obtained within a 2% error for both cases. Indeed, our phantom experiment results are highly consistent with the previous simulation results [24,31].

Most previous studies have been targeting mouse imaging, and therefore noncontact FT systems were generally optimized and validated for small-sized objects [10,36]. For instance, Hervé *et al.* used a 15 mm thick slab phantom [26]. Likewise, Koenig *et al.* utilized an imaging chamber with 15 mm thickness [37]. In this study, we applied 41 mm diameter cylindrical phantoms, which resemble larger animal models such as rat. We also believe that these experimental studies with larger phantoms will pave the way for translation of the FT technique for clinical applications such as breast cancer imaging or brain imaging.

In conclusion, we have built a noncontact CCD-based multiprojectional FT system that could obtain both FT and DOT measurements congruently in the same settings. We evaluated the importance of both functional and structural *a priori* information using multimodality phantoms with different compartments representing heterogeneous optical background. In practice, the functional *a priori* information can be obtained by acquiring additional DOT measurements prior to the FT measurement. In our study, homogeneous scattering coefficient distribution was assumed. However, in reality the scattering coefficient can also be very heterogeneous. In order to effectively separate the absorption and scattering coefficients during the reconstruction, time-dependent DOT measurements are required. This can be achieved by using a frequency-domain or time-domain DOT system. The structural *a priori* information, on the other hand, can be obtained from a high resolution anatomical imaging modality such as MRI, as demonstrated in this paper. It should be noted that other modalities may also be used to obtain structural *a priori* information. A multimodality imaging system that can acquire both structural and functional *a priori* information in the same setting would be preferable due to its superior coregistration potential. Several examples of hybrid systems such as DOT MRI and positron-emission tomography MRI have recently emerged as truly integrated multimodality systems [17,20,38,39]. In essence, our preliminary phantom studies have validated that a system that can acquire DOT, FT, and anatomical images in the same setting would be very promising for quantitative *in vivo* FT.

Acknowledgments

This research is supported in part by the California Institute for Regenerative Medicine, through training grant T1-00008 awarded to Y. Lin, and the National Institutes of Health (NIH) grants R44EB007873 and R01EB008716.

References

1. Ntziachristos V, Ripoll J, Wang LV, Weissleder R. Looking and listening to light: the evolution of whole-body photonic imaging. Nat. Biotechnol 2005;23:313–320. [PubMed: 15765087]
2. Bremer C, Ntziachristos V, Weitkamp B, Theilmeier G, Heindel W, Weissleder R. Optical imaging of spontaneous breast tumors using protease sensing ‘smart’ optical probes. Invest. Radiol 2005;40:321–327. [PubMed: 15905717]
3. Becker A, Hessenius C, Licha K, Ebert B, Sukowski U, Semmler W, Wiedenmann B, Grotzinger C. Receptortargeted optical imaging of tumors with near-infrared fluorescent ligands. Nat. Biotechnol 2001;19:327–331. [PubMed: 11283589]
4. Pu Y, Wang WB, Tang GC, Zeng F, Achilefu S, Vitenson JH, Sawczuk I, Peters S, Lombardo JM, Alfano RR. Spectral polarization imaging of human prostate cancer tissue using a near-infrared receptor-targeted contrast agent. Technol. Cancer. Res. Treat 2005;4:429–436. [PubMed: 16029061]
5. Ntziachristos V. Fluorescence molecular imaging. Annu. Rev. Biomed. Eng 2006;8:1–33. [PubMed: 16834550]
6. Funovics MA, Alencar H, Montet X, Weissleder R, Mahmood U. Simultaneous fluorescence imaging of protease expression and vascularity during murine colonoscopy for colonic lesion characterization. Gastrointest. Endosc 2006;64:589–597. [PubMed: 16996355]
7. Ntziachristos V, Ripoll J, Wang LV, Weissleder R. Looking and listening to light: the evolution of whole-body photonic imaging. Nat. Biotechnol 2005;23:313–320. [PubMed: 15765087]
8. Ntziachristos V, Bremer C, Weissleder R. Fluorescence imaging with near-infrared light: new technological advances that enable *in vivo* molecular imaging. Eur. Radiol 2003;13:195–208. [PubMed: 12541130]
9. Garofalakis A, Zacharakis G, Meyer H, Economou EN, Mamalaki C, Papamatheakis J, Kioussis D, Ntziachristos V, Ripoll J. Three-dimensional *in vivo* imaging of green fluorescent protein-expressing T cells in mice with noncontact fluorescence molecular tomography. Mol. Imaging 2007;6:96–107. [PubMed: 17445504]
10. Graves EE, Ripoll J, Weissleder R, Ntziachristos V. A submillimeter resolution fluorescence molecular imaging system for small animal imaging. Med. Phys 2003;30:901–911. [PubMed: 12772999]
11. Graves EE, Weissleder R, Ntziachristos V. Fluorescence molecular imaging of small animal tumor models. Curr. Mol. Med 2004;4:419–430. [PubMed: 15354872]
12. Arridge SR. Optical tomography in medical imaging. Inverse Probl 1999;15:R41–R93.
13. Boas DA, Brooks DH, Miller EL, DiMarzio CA, Kilmer M, Gaudette RJ, Zhang Q. Imaging the body with diffuse optical tomography. IEEE Signal Process. Mag 2001;18:57–75.
14. Gulsen G, Unlu MB, Birgul O, Nalcioglu O. Simultaneous monitoring of multiple contrast agents using a hybrid MR-DOT system. Proc. SPIE 2007;6431:64310D.

15. Gulsen G, Birgul O, Unlu MB, Shafiiha R, Nalcioglu O. Combined diffuse optical tomography (DOT) and MRI system for cancer imaging in small animals. Technol. Cancer. Res. Treat 2006;5:351–363. [PubMed: 16866566]
16. Arridge SR, Hebden JC. Optical imaging in medicine: II. Modelling and reconstruction. Phys. Med. Biol 1997;42:841–853. [PubMed: 9172263]
17. Brooksby B, Pogue BW, Jiang S, Dehghani H, Srinivasan S, Kogel C, Tosteson TD, Weaver J, Poplack SP, Paulsen KD. Imaging breast adipose and fibroglandular tissue molecular signatures by using hybrid MRI-guided near-infrared spectral tomography. Proc. Natl. Acad. Sci. U.S.A 2006;103:8828–8833. [PubMed: 16731633]
18. Intes X, Maloux C, Guven M, Yazici B, Chance B. Diffuse optical tomography with physiological and spatial a priori constraints. Phys. Med. Biol 2004;49:N155–N163. [PubMed: 15272687]
19. Birgul, O.; Gulsen, G.; Shafiiha, R.; Unlu, MB.; Nalcioglu, O. Biomedical Optics, Technical Digest. Optical Society of America; 2006. *In vivo* small animal imaging using combined MR-DOT system. paper TuG1
20. Gulsen, G.; Unlu, MB.; Birgul, O.; Yan, H.; Nalcioglu, O. A multi-modality system for dynamic imaging of cancer. Proceedings of IEEE Conference on International Symposium on Biomedical Imaging; IEEE; 2006.
21. Guven M, Kwon K, Yazici B, Ntziachristos V. Fluorescence diffuse optical image reconstruction with *a priori* information. Proc. SPIE 2007;6431:643107.
22. Serdaroglu, A.; Yazici, B.; Ntziachristos, V. Fluorescence molecular tomography based on *a priori* information; Biomedical Optics Conference; OSA. 2006.
23. Davis SC, Pogue BW, Springett R, Leussler C, Mazurkewitz P, Tuttle SB, Gibbs-Strauss SL, Jiang SS, Dehghani H, Paulsen KD. Magnetic resonance-coupled fluorescence tomography scanner for molecular imaging of tissue. Rev. Sci. Instrum 2008;79:064302. [PubMed: 18601421]
24. Davis SC, Dehghani H, Wang J, Jiang S, Pogue BW, Paulsen KD. Image-guided diffuse optical fluorescence tomography implemented with Laplacian-type regularization. Opt. Express 2007;15:4066. [PubMed: 19532650]
25. Tan Y, Jiang H. Diffuse optical tomography guided quantitative fluorescence molecular tomography. Appl. Opt 2008;47:2011–2016. [PubMed: 18425173]
26. Hervé L, Koenig A, Silva AD, Berger M, Boutet J, Dinten JM, Peltié P, Rizo P. Noncontact fluorescence diffuse optical tomography of heterogeneous media. Appl. Opt 2007;46:4896–4906. [PubMed: 17676093]
27. Milstein AB, Oh S, Webb KJ, Bouman CA, Zhang Q, Boas DA, Millane RP. Fluorescence optical diffusion tomography. Appl. Opt 2003;42:3081–3094. [PubMed: 12790460]
28. Godavarty A, Thompson AB, Roy R, Gurfinkel M, Eppstein MJ, Zhang C, Sevick-Muraca EM. Diagnostic imaging of breast cancer using fluorescence-enhanced optical tomography. J Biomed. Opt 2004;9:488–496. [PubMed: 15189086]
29. Haskell RC, Svaasand LO, Tsay T, Feng TC, McAdams MS, Tromberg BJ. Boundary conditions for the diffusion equation in radiative transfer. J. Opt. Soc. Am. A 1994;11:2727–2741.
30. Yalavarthy PK, Pogue BW, Dehghani H, Carpenter CM, Jiang H, Paulsen KD. Structural information within regularization matrices improves near infrared diffuse optical tomography. Opt. Express 2007;15:8043. [PubMed: 19547132]
31. Lin Y, Gao H, Nalcioglu O, Gulsen G. Fluorescence diffuse optical tomography with functional and anatomical *a priori* information: feasibility study. Phys. Med. Biol 2007;52:5569–5585. [PubMed: 17804882]
32. Sevick-Muraca EM, Rasmussen JC. Molecular imaging with optics: primer and case for near-infrared fluorescence techniques in personalized medicine. J Biomed. Opt 2008;13:041303. [PubMed: 19021311]
33. Kepshire DS, Davis SC, Dehghani H, Paulsen KD, Pogue BW. Subsurface diffuse optical tomography can localize absorber and fluorescent objects but recovered image sensitivity is nonlinear with depth. Appl. Opt 2007;46:1669–1678. [PubMed: 17356609]
34. Lin Y, Gao H, Nalcioglu O, Gulsen G. Fluorescence diffuse optical tomography with structural *a priori* information: property analysis. Proc. SPIE 2008;6850:35.

35. Da Silva, A.; Bordy, T.; Debourdeau, M.; Dinten, JM.; Peltie, P.; Rizo, P. Coupling x-ray and optical tomography systems for *in vivo* examination of small animals. Proceedings of the 29th Annual International Conference of the IEEE EMBS; IEEE; 2007. p. 3335-3338.

36. Schulz, RB.; Ripoll, J.; Ntziachristos, V. Experimental fluorescence tomography of tissues with noncontact measurements. Proceedings of IEEE Conference on Translational Medical Imaging; IEEE; 2004. p. 492-500.

37. Koenig A, Herve L, Josserand V, Berger M, Boutet J, Da Silva A, Dinten JM, Peltie P, Coll JL, Rizo P. *In vivo* mice lung tumor follow-up with fluorescence diffuse optical tomography. J. Biomed. Opt 2008;13:011008. [PubMed: 18315357]

38. Brooksby B, Jiang S, Dehghani H, Pogue BW, Paulsen KD, Weaver J, Kogel C, Poplack SP. Combining nearinfrared tomography and magnetic resonance imaging to study *in vivo* breast tissue: implementation of a Laplacian-type regularization to incorporate magnetic resonance structure. J. Biomed. Opt 2005;10:051504. [PubMed: 16292948]

39. Judenhofer MS, Wehrl HF, Newport DF, Catana C, Siegel SB, Becker M, Thielscher A, Kneilling M, Lichy MP, Eichner M, Klingel K, Reischl G, Widmaier S, Rocken M, Nutt RE, Machulla HJ, Uludag K, Cherry SR, Claussen CD, Pichler BJ. Simultaneous PET-MRI: a new approach for functional and morphological imaging. Nat. Med 2008;14:459–465. [PubMed: 18376410]

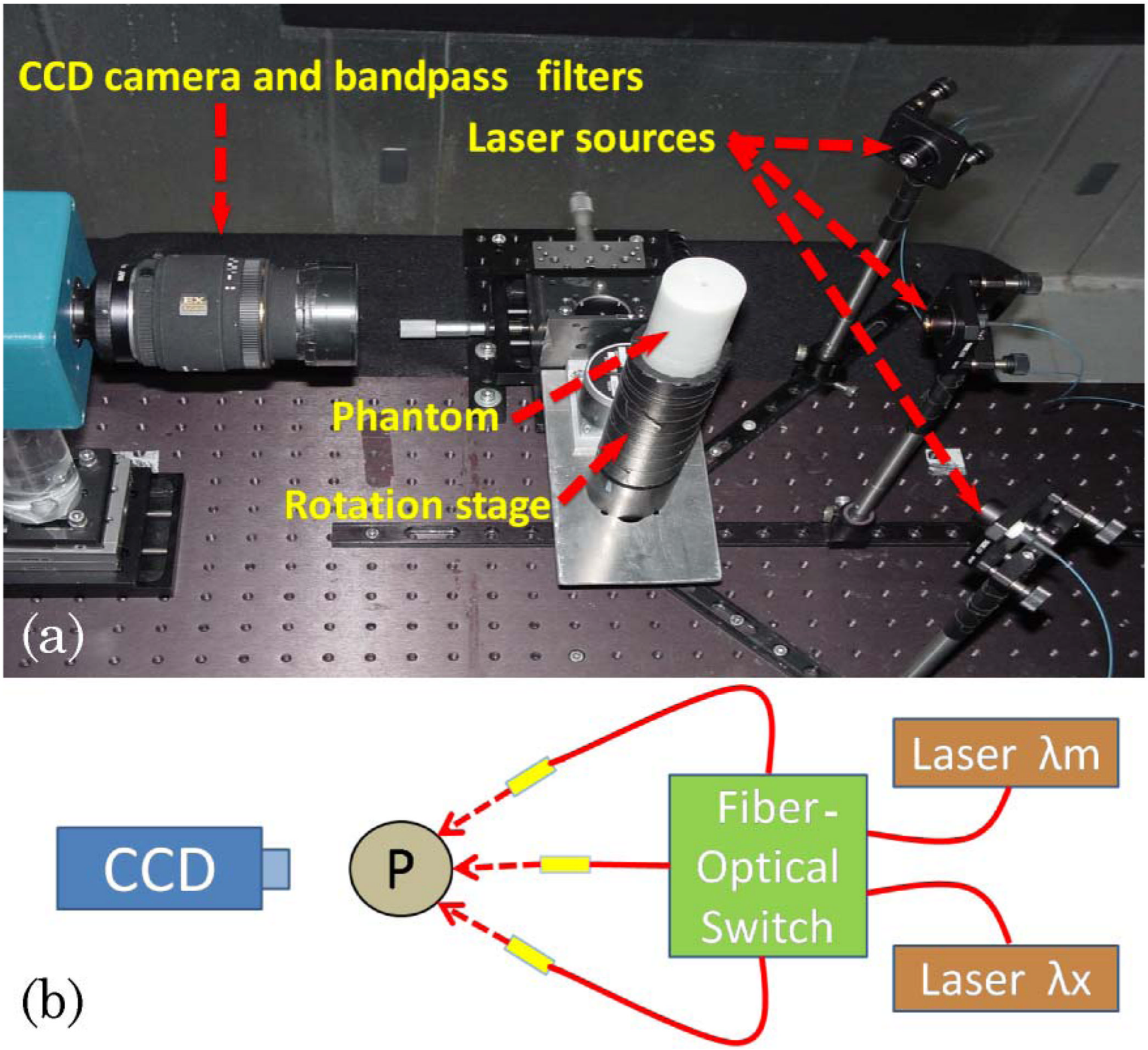

Fig. 1.

(Color online) (a) Photograph of the setup (top view). The CCD camera is on the left-hand side, the cylindrical phantom is placed on a rotation stage, and the phantom is illuminated from one of the three source positions, indicated by arrows. (b) Schematic showing the fiber-optic switch used to illuminate the object (P) from any one of three different positions (L1, L2, and L3). It also allows the selection of either the emission (λm) or the excitation (λx) wavelength.

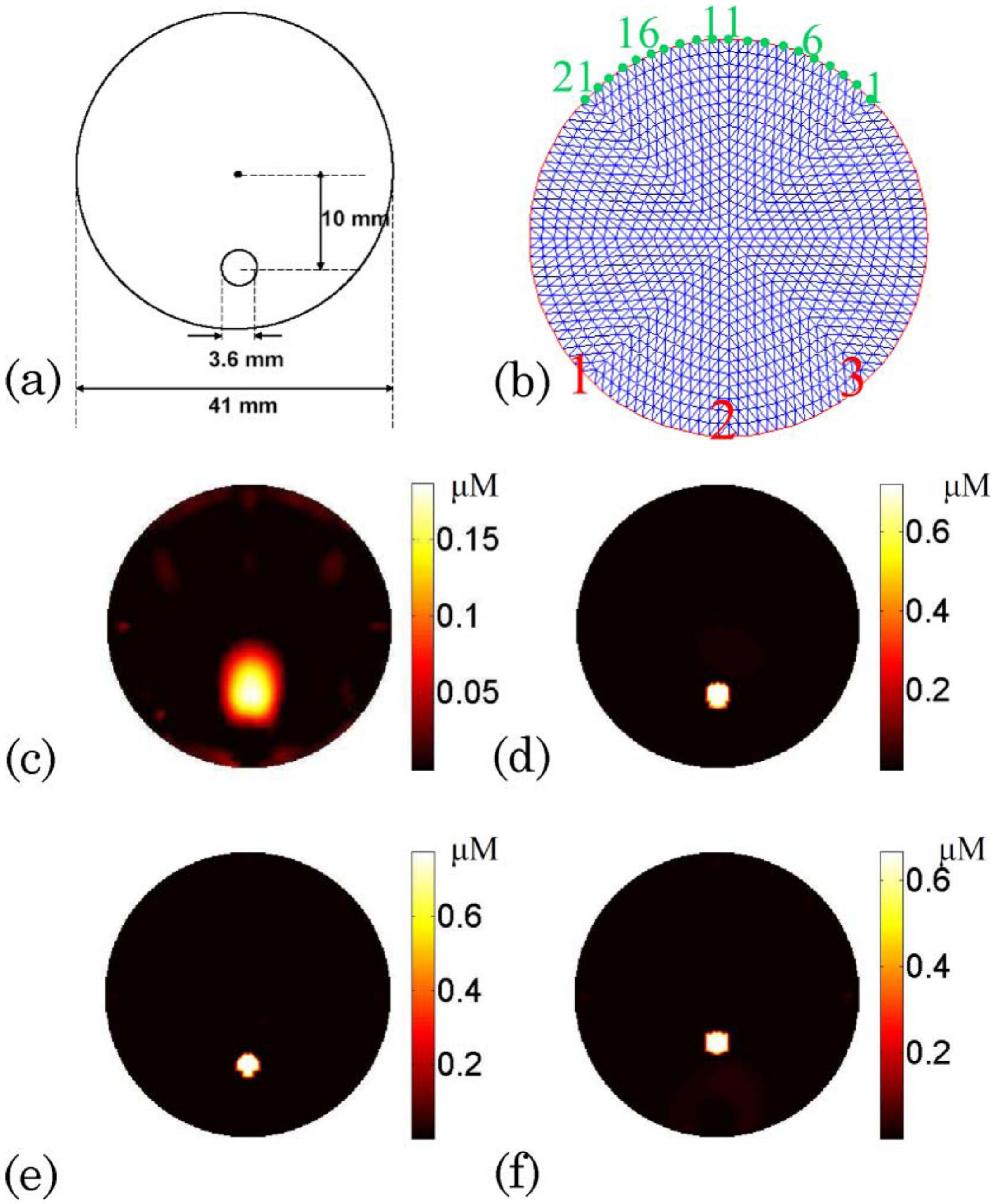

Fig. 2.

(Color online) (a) Schematic showing the 3:6 mm diameter object located 10 mm away from the center of the medium. (b) Schematic showing the three source positions 45° apart from each other (indicated in red numbers). The 21 detectors are equally distributed at the boundaries (indicated in green numbers). (c) Reconstructed fluorophore concentration map for Case 1 without the guidance of structural *a priori* information. Please note that the absorption coefficient of the homogeneous background is found from the DOT measurements and is used as the functional *a priori* information. (d) Reconstructed fluorophore concentration map for Case 1 when the structural *a priori* information is utilized. (e), (f) Reconstructed fluorophore concentration map when the object size is underestimated by 10% and the object location is estimated 3 mm off from the structural images, respectively.

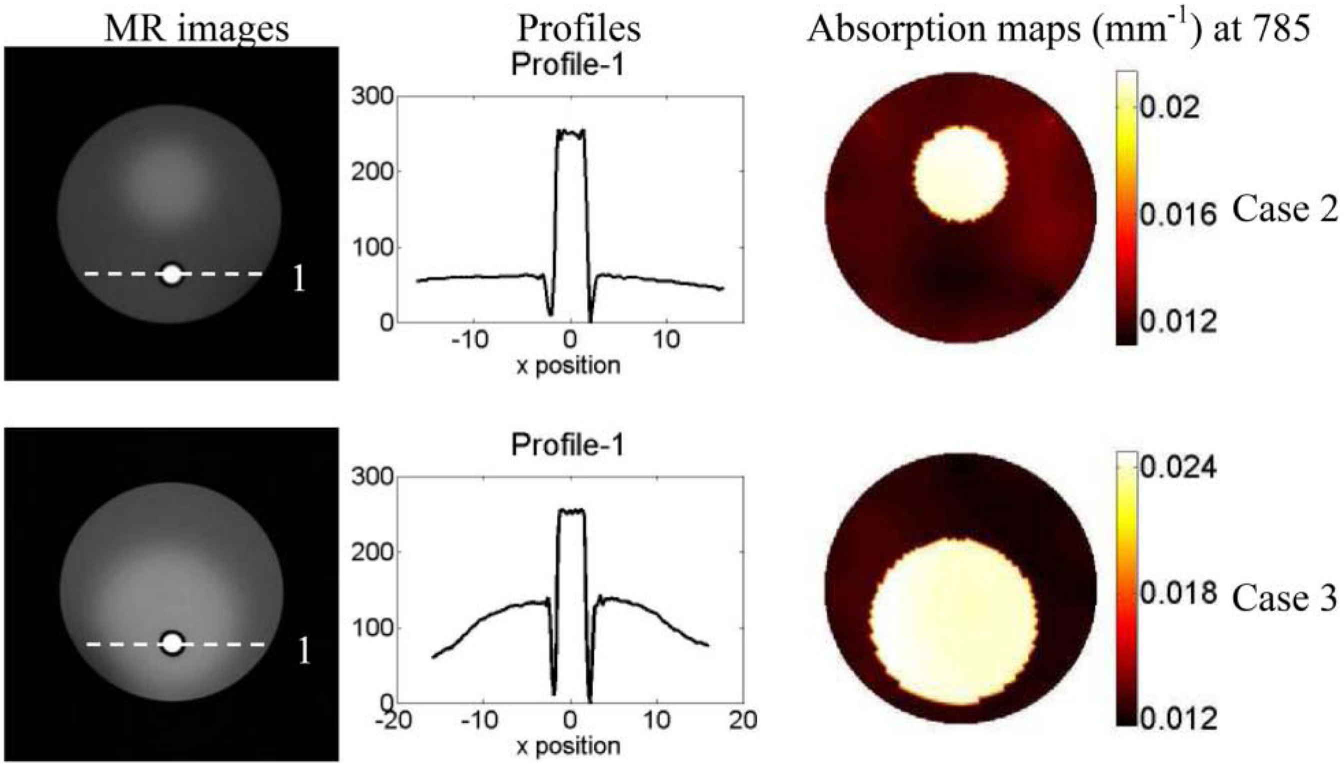

Fig. 3.

(Color online) First column is the T1 weighted MR images of the phantoms for phantom study Cases 2 and 3. The fluorophore is held by a transparent tube with 0:5 mm wall thickness (dark circle shown in MR image). The middle column is the plot of the profile along the *x* axis across the fluorescence object (as indicated by the dashed line in the MR images). The absorption maps at 785 nm are displayed in the third column.

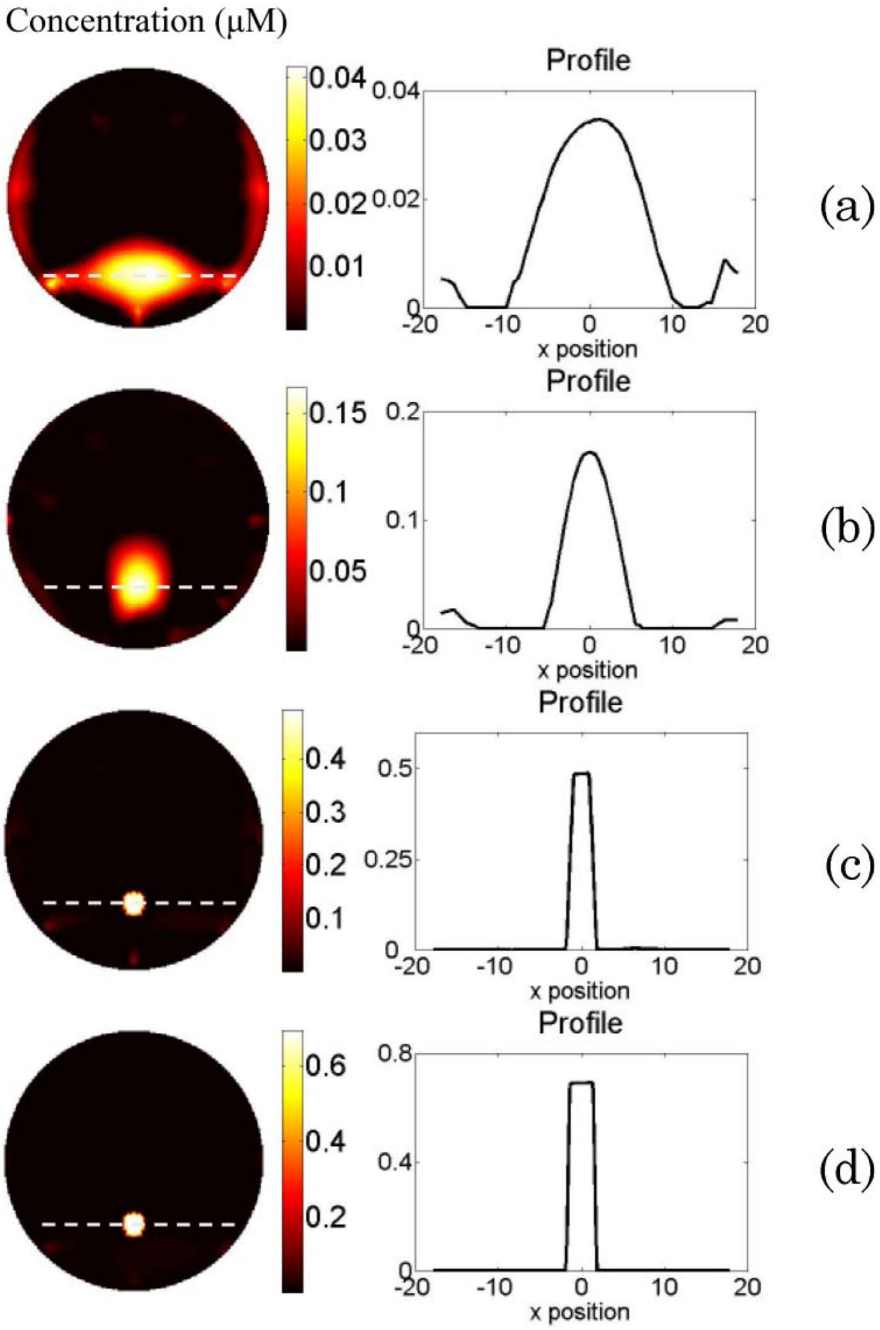

Fig. 4.

(Color online) Phantom study results for Case 2. The reconstructed fluorophore concentration maps are shown in the left column when (a) using erroneous absorption coefficient and disregarding the background heterogeneity; (b) using reconstructed absorption map from DOT measurement as the functional *a priori* information in the FT reconstruction; (c) using erroneous absorption coefficient, disregarding the background heterogeneity, and using only the structural *a priori* information for FT reconstruction; and (d) using reconstructed absorption map as the functional *a priori* information and applying the structural *a priori* information during the FT reconstruction. The right column is the plot of the profile along the *x* axis across the fluorescence object (as indicated by the dashed line in the reconstructed map).

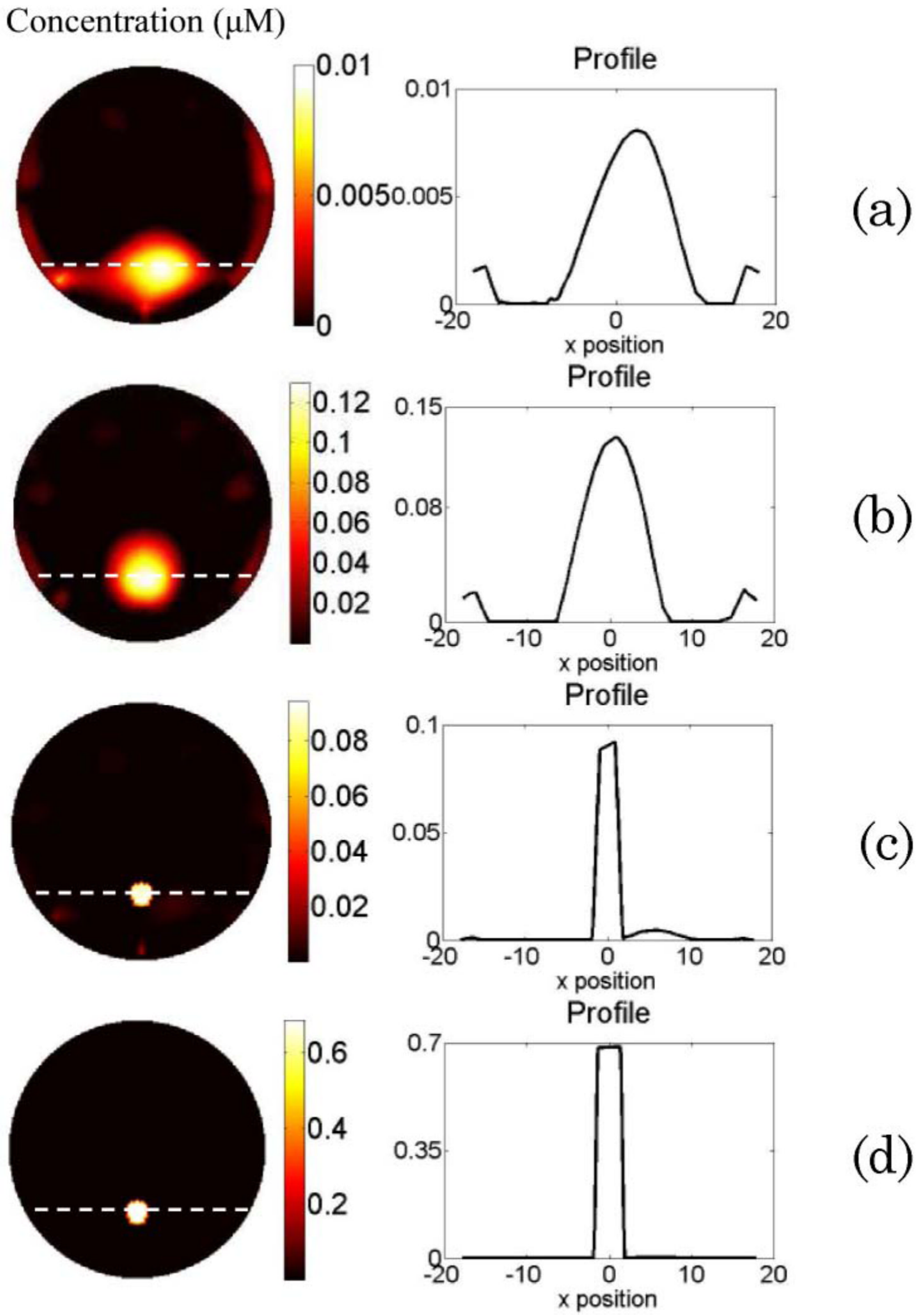

Fig. 5.

(Color online) Phantom study results for Case 3. The reconstructed fluorophore concentration maps are shown in the left column when (a) using erroneous absorption coefficient and disregarding the background heterogeneity; (b) using reconstructed absorption map from DOT measurement as the functional *a priori* information in the FT reconstruction; (c) using erroneous absorption coefficient, disregarding the background heterogeneity, and using only the structural *a priori* information for FT reconstruction; (d) using reconstructed absorption map as the functional *a priori* information and applying the structural *a priori* information during the FT reconstruction. The right column is the plot of the profile along the *x* axis across the fluorescence object (as indicated by the dashed line in the reconstructed map).

Table 1

Phantom Study Results for Cases 2 and 3[a]

	True	A	B	C	D
Case 2	0.67	0.033	0.13	0.48	0.67
Case 3	0.67	0.007	0.11	0.09	0.69

[a] Fluorophore concentration is in μM. Columns A, B, C, and D reflect (a), (b), (c), and (d), respectively, of Fig. 4 and Fig. 5.